CHEMISTRY OF MATERIALS
Article

Chem. Mater. **2010,** *22,* 5463–5473 5463
DOI:10.1021/cm101072z

Synthesis and Electrochemical Performance of Heteroatom-Incorporated Ordered Mesoporous Carbons

Xiaochen Zhao,[†,‡] Aiqin Wang,[†] Jingwang Yan,[§] Gongquan Sun,[§] Lixian Sun,[†] and Tao Zhang*[,†]

[†]*State Key Laboratory of Catalysis, and* [§]*Laboratory of Fuel Cell, Dalian Institute of Chemical Physics, Chinese Academy of Sciences, Zhongshan Road 457, Dalian 116023, P. R. China, and* [‡]*Graduate University of Chinese Academy of Sciences, Beijing 100049, P. R. China*

Received April 17, 2010. Revised Manuscript Received August 4, 2010

Heteroatom-incorporated 2D ordered mesoporous carbons (OMCs) were fabricated via a one-pot organic−organic aqueous self-assembly approach, using resorcinol (R) and formaldehyde (F) as the carbon precursor and triblock copolymer Pluronic F127 as the mesoporous structure template. In this approach, RF resin, boric acid and/or phosphoric acid, and F127 underwent a self-assembly process under a strong acidic condition to form a polymer with ordered mesostructure, which was then carbonized at 800 °C in a nitrogen atmosphere to form B-incorporated, P-incorporated, or B, P-coincorporated OMCs. Nitrogen sorption, X-ray diffraction (XRD), and transmission electron microscopy (TEM) revealed that the heteroatom-incorporated OMCs possessed highly ordered mesoporous structures, uniform pore size distributions, and large surface areas ranging from 500 to 700 m^2/g. The incorporation of heteroatoms effectively limited the framework shrinkage during the carbonization process, and simultaneously increased the surface oxygen groups in the carbons. The resulting heteroatom-incorporated OMCs exhibited superior electrochemical performances to nonincorporated counterpart when used as electrodes of supercapacitors.

Introduction

Porous carbon-based supercapacitors have been regarded as one of the most promising electric power sources due to their high power density and long cycle life.[1,2] The performance of supercapacitors strongly depends on the textural properties of the porous carbon electrodes, such as surface area, pore size distribution, and tortuosity of pores. Activated carbon is the most widely used electrode material for supercapacitors because of its large surface area, good conductivity, and low cost. Unfortunately, the presence of ultramicropores that are inaccessible to the electrolyte ions, as well as the broad distribution of pore size, significantly lowers the specific capacitance of the activated carbon. Ordered mesoporous carbons (OMCs), on the other hand, with uniform and tunable pore sizes and fast accessibility of large electrolyte ions, seem to be attractive candidates as electrode materials for supercapacitors. Especially, under high rate, short duration, and power pulse discharge or recharge, OMCs offer significant advantages over the microporous activated carbon.

To enhance further the capacitance of the supercapacitors, we introduced surface functionalities into the porous carbon electrodes. Many studies on carbon materials have shown that modification with electron-donating or electron-withdrawing elements, such as N,[3−6] P,[7,8] B,[9,10] and O,[11] could change the electronic properties of carbons and produce additional functional groups on the carbon surface, and as a result, greatly enhance the electrochemical performances of carbon materials. In most cases, however, the modifying process is accomplished by post-treatment of the preformed carbon materials,[6,7,10] which is simple but less controllable in either the amount or distribution of dopants. Especially in the case of OMCs, the post-treatment process may bring about partial or even complete destruction of the ordered mesoporous structure, which is undesirable in applications.[12,13] Therefore, one would expect to directly incorporate heteroatoms into the

*Corresponding author. Fax: +86-411-84691570. Tel: +86-411-84379015. E-mail: taozhang@dicp.ac.cn.

(1) Conway, B. E. *Electrochemical Supercapacitors: Scientific Fundamentals and Technological Applications*; Kluwer Academic/Plenum: New York, 1999.
(2) Simon, P.; Gogotsi, Y. *Nat. Mater.* **2008**, *7*, 845.
(3) Hulicova-Jurcakova, D.; Kodama, M.; Shiraishi, S.; Hatori, H.; Zhu, Z. H.; Lu, G. Q. *Adv. Funct. Mater.* **2009**, *19*, 1800.
(4) Xia, Y.; Mokaya, R. *Adv. Mater.* **2004**, *16*, 1553.
(5) Liang, Y.; Feng, X.; Zhi, L.; Kolb, U.; Mullen, K. *Chem. Commun.* **2009**, 809.
(6) Kim, N. D.; Kim, W.; Joo, J. B.; Oh, S.; Kim, P.; Kim, Y.; Yi, J. *J. Power Sources* **2008**, *180*, 671.
(7) Zhang, J.; Liu, X.; Blume, R.; Zhang, A.; Schlogl, R.; Su, D. S. *Science* **2008**, *322*, 73.
(8) Hulicova-Jurcakova, D.; Puziy, A. M.; Poddubnaya, O. I.; Suarez-Garcia, F.; Tascon, J. M. D.; Lu, G. Q. *J. Am. Chem. Soc.* **2009**, *131*, 5026.
(9) Durkic, T.; Peric, A.; Lausevic, M.; Dekanski, A.; Neskovic, O.; Veljkovic, M.; Lausevic, Z. *Carbon* **1997**, *35*, 1567.
(10) Abramovic, B. F.; Bjelica, L. J.; Gaal, F. F.; Guzsvany, V. J.; Jovanovic, L. S. *Electroanalysis* **2003**, *15*, 878.
(11) Oda, H.; Yamashita, A.; Minoura, S.; Okamoto, M.; Morimoto, T. *J. Power Sources* **2006**, *158*, 1510.
(12) Martinhopkins, M. B.; Gilpin, R. K.; Jaroniec, M. *J. Chromatogr. Sci.* **1991**, *29*, 147.
(13) Bahr, J. L.; Tour, J. M. *J. Mater. Chem.* **2002**, *12*, 1952.

Published on Web 09/13/2010

carbon precursors before carbonization, which will afford the possibility for homogeneous distribution of heteroatoms while maintaining the ordered mesoporous structure.

There are two typical approaches for fabricating OMCs: nanocasting method with ordered mesoporous silica as the hard template[14,15] and organic−organic self-assembly method with surfactants as the soft template and phenolic resin as the carbon source.[16−18] Recently, Wang et al. successfully prepared boron- doped mesoporous carbon (MC) by nanocasting method, i.e., filling the mesopores of SBA-15 with a mixture of sucrose and boric acid followed by high-temperature carbonization and removal of silica template with NaOH solution.[19] Although the resulting B-containing mesoporous carbon manifests good electrochemical property as electrodes of supercapacitor, the hard templating method involves multisteps and is unable to be scaled up for mass production. On the other hand, the organic−organic self-assembly approach has shown significant advantages over nanocasting process in terms of simplified procedure and mass production.[20] Moreover, this soft-templating method has achieved great success in fabricating metal- or metal oxide-carbon nanocomposites.[21−27] Very recently, mesoporous melamine resins which have a high content of N (C/N molar ratio equals to 1.65) have been successfully fabricated using hexamethoxymethyl melamine (HMMM) as monomer and block-co-polymer F127 as template.[28] Feng et al. also prepared N-doped OMCs via a self-assembly method.[29] However, up to now, there have not been any reports on the synthesis of B- and/or P-incorporated OMCs by such a multicomponent self-assembly method, although these heteroatom-incorporated OMCs have great potentials in electrochemical applications.

Herein, we for the first time report the synthesis of B-incorporated OMCs, P-incorporated OMCs, and B, P-coincorporated OMCs via a facile one-pot aqueous self-assembly strategy. The electrochemical properties of the heteroatom-incorporated OMCs were evaluated as electrodes of supercapacitors. It was found that the specific capacitance (F/m^2) of the OMC was increased by more than 50% through coincorporation of B and P. More interesting, the B, P-coincorporated OMC exhibited significantly improved capacitance retention at a high potential scan rate, which is desirable in tough power supply conditions.

Experimental Section

Chemicals. Pluronic F127 ($EO_{106}PO_{70}EO_{106}$) was supplied by Sigma-Aldrich and has an average molecular weight of 12600. Resorcinol, formaldehyde (37 wt %), HCl (37 wt %), boric acid, and phosphoric acid (85 wt %) were all supplied by chemical plants in China. All the reagents were used as received without further purification. Deionized water was used in all experiments.

Synthesis Procedure of Heteroatom-Incorporated Ordered Mesoporous Carbons. For a typical synthesis of boron-incorporated OMC (B-OMC), 3.3 g (0.03 mol) of resorcinol and 0.93 g of (0.015 mol) of boric acid were dissolved in a solution containing 15 g of water, 15 g of ethanol, and 2.5 g of F127 under magnetic stirring until the solution turned transparent. Then, 0.8 g of HCl (37 wt %) was added to the solution as a catalyst and stirred for another 1 h. To the above solution was added 3.0 g of formaldehyde (37 wt %) dropwise and stirring was maintained for 1.5 h. The transparent homogeneous mixture was aged at room temperature for 96 h until it turned cloudy and separated into two phases finally. The upper layer was discarded, whereas the lower one was retained and stirred to form a sticky monolith. Afterward, the sticky monolith was kept standing for 2 days at room temperature until it turned transparent again. The monolith was cured at 80 °C for 2 days, and then heated under a N_2 atmosphere at 350 °C for 2 h to remove surfactant and followed by carbonization at 800 °C for 2 h, at a ramping rate of 1 °C/min. The final product is denoted as B0.5-OMC, where 0.5 represents the atomic ratio of boric acid to resorcinol. Phosphorus-incorporated OMCs (P-OMCs) were obtained via a similar approach as the synthesis of B-OMC except by replacing boric acid with phosphoric acid. For the synthesis of B, P-coincorporated OMCs (BP-OMCs), the amount of F127 was increased to 3.0 g, whereas that of HCl was decreased to 0.6 g in addition to replacing boric acid with a mixture of boric acid and phosphoric acid. By varying the amount of boric acid and phosphoric acid, the B-OMCs, P-OMCs, and B, P-OMCs with different concentrations of heteroatoms were fabricated and denoted as B*m*-OMC, P*n*-OMC, and B*m*P*n*-OMC, respectively (where m or n represents the atomic ratio of boric acid or phosphoric acid to resorcinol). In some control experiments, the reaction temperature was varied from 25 °C (room temperature) to 60 °C, the aging time was varied from 48 to 96 h, and the amounts of F127 and HCl were varied from 2 to 4 g and from 0.3 to 1.2 g, respectively. For comparison, the nonincorporated OMC was also prepared according to our previous work.[22]

Characterizations. Nitrogen adsorption−desorption measurements were performed at −196 °C with a Micromeritics ASAP2010 instrument. Prior to the measurements, the samples were degassed at 110 °C for 1 h and at 250 °C for 4 h. The specific surface areas (S_{BET}) were calculated with BET equation, the total pore volumes (V_P) were determined at P/P_0 of 0.995, and the average pore diameters (D_P) were estimated with adsorption branches based on BJH model while the micropore distributions were obtained by H−K equation. X-ray diffraction (XRD) patterns were collected on a PW3040/60 X' Pert PRO (PANalytical) diffractometer equipped with a Cu Kα radiation

(14) Ryoo, R.; Joo, S. H.; Jun, S. *J. Phys. Chem. B* **1999**, *103*, 7743.
(15) Shin, H. J.; Ryoo, R.; Kruk, M.; Jaroniec, M. *Chem. Commun.* **2001**, 349.
(16) Liang, C.; Dai, S. *J. Am. Chem. Soc.* **2006**, *128*, 5316.
(17) Zhang, F. Q.; Meng, Y.; Gu, D.; Yan, Y.; Yu, C. Z.; Tu, B.; Zhao, D. Y. *J. Am. Chem. Soc.* **2005**, *127*, 13508.
(18) Wang, X.; Liang, C.; Dai, S. *Langmuir* **2008**, *24*, 7500.
(19) Wang, D. W.; Li, F.; Chen, Z. G.; Lu, G. Q.; Cheng, H. M. *Chem. Mater.* **2008**, *20*, 7195.
(20) Liang, C.; Li, Z.; Dai, S. *Angew. Chem., Int. Ed.* **2008**, *47*, 2.
(21) Wang, H.; Wang, A.; Wang, X.; Zhang, T. *Chem. Commun.* **2008**, 2565.
(22) Gao, P.; Wang, A.; Wang, X.; Zhang, T. *Chem. Mater.* **2008**, *20*, 1881.
(23) Gao, P.; Wang, A.; Wang, X.; Zhang, T. *Catal. Lett.* **2008**, *125*, 289.
(24) Li, J. S.; Gu, J.; Li, H. J.; Liang, Y.; Hao, Y. X.; Sun, X. Y.; Wang, L. J. *Microporous Mesoporous Mater.* **2010**, *128*, 144.
(25) Yao, J. Y.; Li, L. X.; Song, H. H.; Liu, C. Y.; Chen, X. H. *Carbon* **2009**, *47*, 436.
(26) Liu, R. L.; Shi, Y. F.; Wan, Y.; Meng, Y.; Zhang, F. Q.; Gu, D.; Chen, Z. X.; Tu, B.; Zhao, D. Y. *J. Am. Chem. Soc.* **2006**, *128*, 11652.
(27) Liu, R.; Ren, Y.; Shi, Y.; Zhang, F.; Zhang, L.; Tu, B.; Zhao, D. *Chem. Mater.* **2008**, *20*, 1140.
(28) Kailasam, K.; Jun, Y. S.; Katekomol, P.; Epping, J. D.; Hong, W. H.; Thomas, A. *Chem. Mater.* **2010**, *22*, 428.
(29) Feng, C.; Li, H.; Wan, Y. *J. Nanosci. Nanotechnol.* **2009**, *9*, 1558.

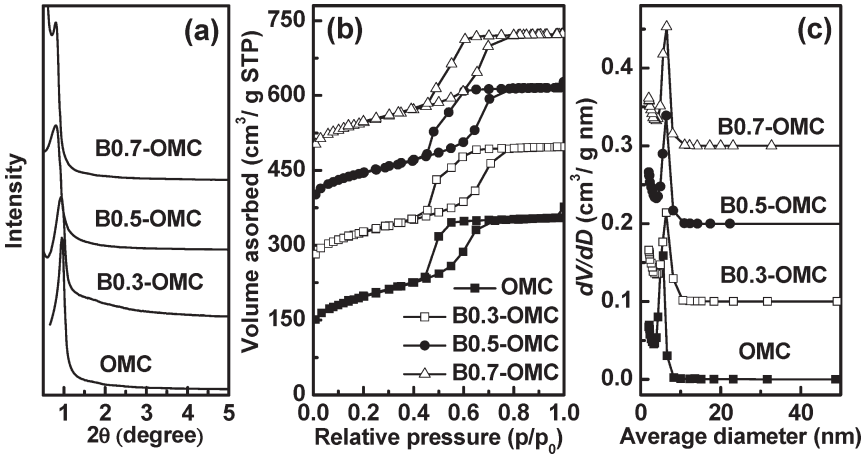

Figure 1. (a) Low-angle XRD patterns, (b) N_2 sorption isotherms, and (c) pore size distributions of B-incorporated OMCs and OMC. The isotherms of each sample in one diagram are offset vertically by 120 cm^3/g and the BJH curves of each sample in one diagram are offset vertically by 0.1 cm^3/g nm.

source (λ = 0.15432 nm). A continuous mode was used for collecting data in the 2θ range from 0.5 to 4.5° operating at 40 kV, 30 mA and from 10 to 80° operating at 40 kV, 40 mA. Transmission electron microscopy (TEM) images were obtained on a Tecnai G^2 Spirit FEI transmission electron microscope operating at 120 kV, and electron energy loss spectroscopy (EELS) mapping images were obtained on a Tecnai G^2 F30 S-Twin Transmission Electron Microscope operating at 300 kV. A few droplets of a sample suspension in ethanol were put on a microgrid carbon polymer supported on a copper grid for TEM and EELS examinations. X-ray photoelectron spectroscopy (XPS) was conducted on ESCALAB250 (Thermo VG Corporation) equipped with an Al Kα radiation source (1486.6 eV, 15 kV, 10 mA, 150 W). All binding energies (B.E.) were calibrated with graphitic carbon C1s peak at B.E. of 284.5 eV as a reference. The recorded spectra were fitted by a least-squares procedure to a product of Gaussian−Lorentzian functions after subtraction of background noise. The concentration of each element was calculated from the area of the corresponding peak calibrated with the atomic sensitivity factor using C as reference. Thermogravimetry (TG) was performed on a Setaram Setsys 16/18 thermoanalyzer with a heating rate of 2 °C/min in N_2 flow.

Electrochemical Measurements. For preparing a working electrode, a mixture of an active material, carbon black, and poly(tetrafluoroethylene) (PTFE) with a weight ratio of 90:5:5 was ground together to form a homogeneous slurry. The slurry was squeezed into a film and then punched into pellets with a surface area of 1 cm^2 for each piece. The punched pellets with a piece of nickel foam on each side were pressed under 6 MPa and dried overnight at 120 °C. Prior to the electrochemical tests, the electrodes were impregnated with electrolyte under vacuum for several hours. The cyclic voltammetry (CV) tests were conducted using a Zahner Elektrik IM6e electrochemical workstation in a three-electrode cell system, employing a sintered $Ni(OH)_2$/NiOOH as the counter electrode, a Hg/HgO as the reference electrode and a 6 M KOH solution as the electrolyte. Scan rates of 2, 5, 10, 20, 50, and 100 mV/s were applied in the CV studies. The Galvanostatic charge−discharge (GC) measurements were conducted on an automatic LAND battery test instrument (CT2001A) to evaluate the charge/discharge performance. A current of 0.2 A/g was applied in GC studies. The specific capacitance (F/g) was calculated as $C = (I\Delta t)/\Delta U$, where I is the discharge current in Amperes per gram of active material, Δt is the discharge time in second, and ΔU is the voltage window from the end of the IR drop to the end of the discharge process in volts. The calculations were per single electrode of the obtained materials according to GC test at a current of 0.2 A/g. In some cases, C is presented as F/m^2, which is obtained according to the equation C (F/m^2) = C (F/g)/S_{BET}. Capacitance retention (R) is defined as the ratio of capacitance at a potential scan rate of 100 mV/s to that at 2 mV/s.

Results and Discussion

Structure Characterization. Figure 1a presents the low-angle XRD patterns of B0.3-OMC, B0.5-OMC, and B0.7-OMC materials in comparison with blank OMC. For the four samples, there is a strong peak at 2θ = 0.5−1° that can be indexed as reflection of (100) of a 2D *p6mm* hexagonal mesostructure. Moreover, the (100) peaks of the B*m*-OMC samples have a shift toward low-angles in comparison with the blank OMC, indicating the B*m*-OMC samples have larger cell parameters than the blank OMC. Panels b and c in Figure 1 show the N_2-sorption isotherms and pore size distributions. The B*m*-OMC samples show typical type IV isotherms with well-defined H1 hysteresis loops, characteristic of mesoporous structure. The pore size distributions are very narrow. Table 1 summarizes the textural parameters and elemental analysis results of the samples synthesized at typical conditions as described in Experimental Section. It can be seen that both B0.3-OMC and B0.5-OMC possess almost the same BET surface areas as the blank OMC, around 700 m^2/g. However, incorporation of too much B (e.g., B0.7-OMC) led to a decrease in the specific surface area of OMC. On the other hand, both the average pore sizes (D_P) and the cell parameters (a_0) of the B*m*-OMCs have an increase as compared to that of OMC, suggesting that the incorporation of B limits the shrinkage of the mesostructures of carbons that occurred during pyrolysis. It was reported that incorporation of metal or metal oxide into the carbon framework could suppress the framework shrinkage.[22,26] Apparently, we now demonstrate that the incorporation of nonmetal elements brought about the same effect. ICP analyses show that the weight concentrations of B in the B*m*-OMC materials are 0.22, 0.32, and 0.56 wt % for B0.3-OMC, B0.5-OMC, and B0.7-OMC,

Table 1. Structural Parameters, Heteroatom Contents, and Specific Capacitance of B*m*-OMCs, P*n*-OMCs, and B*m*P*n*-OMCs

sample	S_{BET} (m^2/g)	S_{micro} (m^2/g)	V_p (cm^3/g)	V_{micro} (cm^3/g)	D_p (nm)	a_0[a] (nm)	contents of heteroatom (wt %)[b] B	P	C[c] (F/m^2)
OMC	702	316	0.63	0.15	4.7	10.5			0.16
B0.3-OMC	707	374	0.58	0.17	4.9	10.9	0.22		0.16
B0.5-OMC	707	372	0.60	0.17	5.0	11.8	0.32		0.19
B0.7-OMC	641	308	0.56	0.14	4.9	12.2	0.56		0.21
P0.3-OMC	614	323	0.59	0.15	5.8	12.3		0.90	0.20
P0.5-OMC	610	330	0.57	0.15	5.9	12.5		1.42	0.24
P0.7-MC	550	306	0.54	0.14	6.5			2.12	0.28
B0.5P0.3-OMC	689	346	0.63	0.16	5.2	11.2	0.43	1.13	0.22
B0.5P0.5-OMC	677	269	0.66	0.12	4.9	11.4	0.67	2.29	0.25
B0.5P0.7-OMC	572	261	0.57	0.12	5.4	11.4	0.60	2.20	0.28
B0.3P0.5-OMC	679	345	0.58	0.16	4.9	11.1	0.31	1.50	0.24
B0.7P0.5-OMC	598	243	0.62	0.11	5.4	11.5	0.77	1.87	0.25
B0.4P0.4-OMC	692	330	0.62	0.15	5.0	11.2	0.43	1.73	0.25
B0.7P0.7-OMC	589	210	0.63	0.10	5.2	11.4	0.97	2.92	0.26
Norit	709	451	0.25	0.21					0.15

[a] a_0 is the cell parameter calculated as $a_0 = 2d_{(100)}/\sqrt{3}$. [b] Determined by ICP. [c] Capacitance was calculated as $C = (I\Delta t)/(\Delta U S_{BET})$, where I is the discharge current in Amperes per gram of active material, Δt is the discharge time in second, ΔU is the voltage window from the end of the IR drop to the end of the discharge process in volt, and S_{BET} is the specific surface area (m^2/g) of the active material. The calculations were per single electrode of the obtained materials according to GC test at a current of 0.2 A/g.

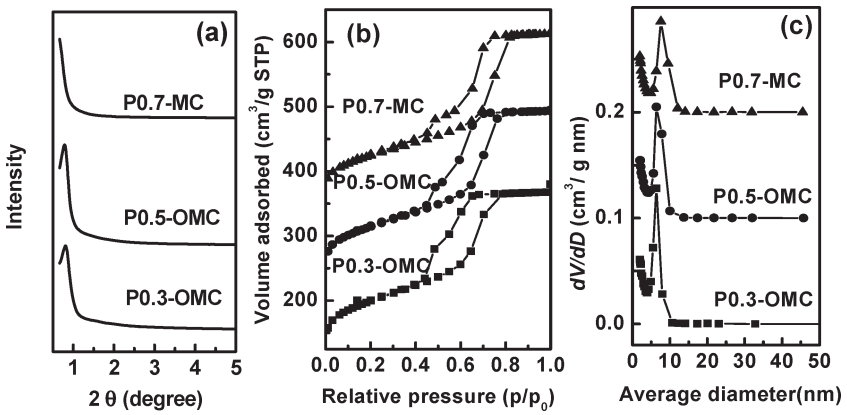

Figure 2. (a) Low-angle XRD patterns, (b) N_2 sorption isotherms, and (c) pore size distributions of P-incorporated OMCs. The isotherms of each sample in one diagram are offset vertically by 120 cm^3/g and BJH curves of each sample in one diagram are offset vertically by 0.1 cm^3/g nm.

respectively. In comparison with the boron-doped mesoporous carbon (BMC) synthesized by hard-templating approach,[19] the B concentrations in our samples are almost two times larger.

Figure 2a shows the low-angle XRD patterns of P*n*-OMCs. Although the strong reflection of (100) is clearly observed in P0.3-OMC and P0.5-OMC samples, no any reflection peaks are found when n equals to 0.7, suggesting that a high content of P introduction, whose atom size is much bigger than carbon, may induce a deterioration of the long-range structural order. The N_2-sorption isotherms shown in Figure 2b are very similar to those of B*m*-OMCs, which are characteristic of mesoporous structures. On the other hand, the pore size distributions become wider with increasing concentration of P (Figure 2c). Different from B*m*-OMCs, P*n*-OMCs show reduced BET surface areas as compared with blank OMC (Table 1). In particular for the P0.7-MC, the BET surface area is only 550 m^2/g. The average pore sizes of the P*n*-OMCs are remarkably larger than those of B*m*-OMCs and OMC. The P contents in the P*n*-OMCs vary from 0.90 to 2.12 wt % when the atomic ratio of phosphoric to resorcinol in the preparation recipe changes from 0.3 to 0.7.

Figure 3 shows the low-angle XRD patterns, N_2-sorption isotherms, and pore size distributions of B, P-coincorporated OMCs. They are similar to those of B*m*-OMC and P*n*-OMC, characterized with one peak in the low-angle XRD patterns, well-defined H1 hysteresis loops, and very narrow pore size distributions. In particular, even with a high concentration of both B and P, e.g., B0.7P0.7-OMC, the ordered mesoporous structure is well-preserved. From Table 1, one can see that the BET surface areas of the B*m*P*n*-OMCs are between 570 and 700 m^2/g depending on the incorporated amount of B and P; especially, the incorporation of P led to decrease in the surface areas. An interesting phenomenon is that the actual contents of B and P in the coincorporated samples are higher than that in the solo-incorporated counterparts. For example, the actual contents of B and P in the B0.5P0.5-OMC are 0.67 and 2.29 wt %, respectively, whereas the B content in the B0.5-OMC is only 0.32 wt % and the P content in the P0.5-OMC is only 1.42 wt %. This result suggests that coincorporation of B and P facilitates the incorporation of them into the carbon framework. To further investigate these B*m*P*n*-OMCs, we fixed the value of *m* at 0.5 and varied *n* from 0.3 to 0.7

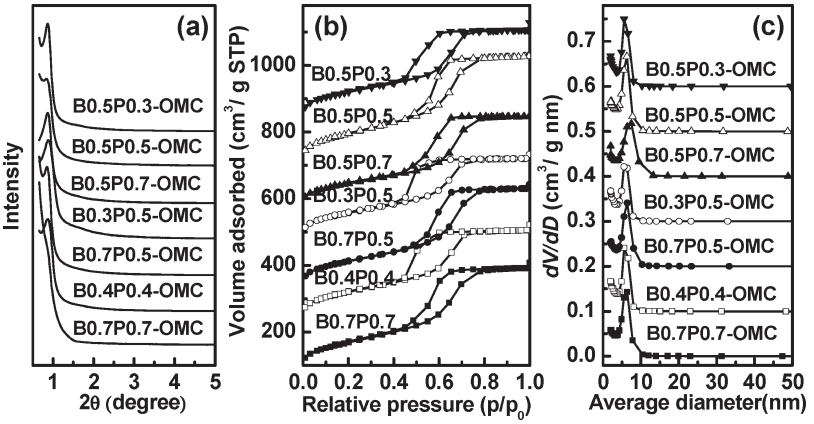

Figure 3. (a) Low-angle XRD patterns, (b) N_2 sorption isotherms, and (c) pore size distributions of B, P-coincorporated OMCs. The isotherms of each sample in one diagram are offset vertically by 120 cm^3/g and the BJH curves of each sample in one diagram are offset vertically by 0.1 cm^3/g nm.

or vice versa. The results in Table 1 show that when m equals to n, the resulting materials have the highest actual contents of B and P. To explain this result, we examined the carbon precursor, i.e., the polymers containing both B and P by using wide-angle XRD technique. As shown in Figure 4, neither the blank polymer (OMP) nor the P-incorporated polymer (P0.5-OMP) shows obvious diffraction peaks in the wide-angle XRD patterns. However, when B was incorporated, the resulting B0.5-OMP shows two weak peaks at around $2\theta = 14.5$ and 28.0°, indicating that a small quantity of hydrogen borate exists (reference code 00−030−0620). Quite differently, when B and P were coincorporated, the resulting sample B0.5P0.5-OMP displays two peaks at around $2\theta = 24.4$ and 39.8°, which can be indexed as reflections of the (101) and (112) planes of boron phosphate (BPO_4, reference code 00−014−0696). This result indicates that when B and P were cointroduced into the RF polymer, boron phosphate was formed. The formation of boron phosphate could explain why both B and P incorporated into the carbon framework reached the highest concentration when the atomic ratio of the two elements was 1 to 1. It should be mentioned that upon carbonization, the XRD peaks corresponding to boron phosphate or hydrogen borate disappeared completely, indicating they decomposed at a high temperature.

Figure 5 shows the representative TEM images of Bm-OMCs, Pn-OMCs, and BmPn-OMCs (m and n vary from 0.3 to 0.7). Long 1D channels along the (100) direction as well as hexagonally arranged pores along the (001) direction (insets) are clearly observed for most of the samples, indicating that ordered mesoporous structures remain well after the incorporation of B and/or P. The only exception is for P0.7-MC, which shows wormholelike structure, in agreement with its low-angle XRD pattern. The pore sizes, measured in TEM images, are also consistent with those calculated by BJH method using N_2-adsorption branches. It should be pointed out that the simultaneous incorporation of B and P not only increased the actual concentration of B and P in the materials, but also facilitated the formation of mesoporous structure. Even for the B0.7P0.7-OMC, a well-ordered mesostructure was obtained.

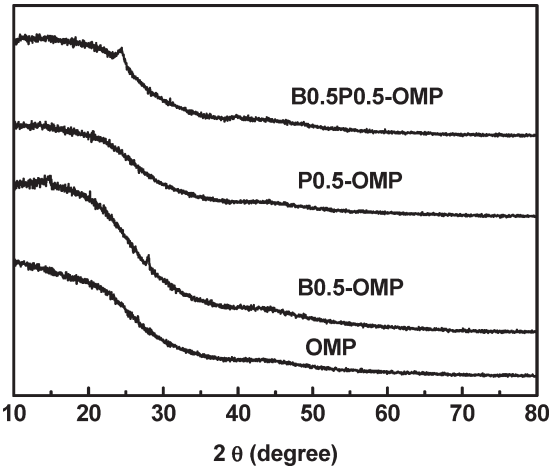

Figure 4. Wide-angle XRD patterns of OMP, B0.5-OMP, P0.5-OMP, and B0.5P0.5-OMP.

EELS is surface-sensitive technique to map light elements such as B and O.[19] Therefore, taking the sample B0.5P0.5-OMC as an example, we performed EELS experiment in order to reveal the distribution of heteroatoms B and P on the carbon surface. The mapping images (Figure 6) indicate that B, P, and O are homogeneously distributed on both the exterior and interior surfaces of OMCs.

It has been shown that the incorporation of B and P suppresses the framework shrinkage of mesoporous carbons during pyrolysis. To understand this process, we conducted TG analysis of the selected four samples in N_2 atmosphere from room temperature to 800 °C. As shown in Figure 7, there are four stages in the TG profiles. The first stage occurred at around 120 °C and was due to loss of water, and the second one was observed between 200 and 300 °C, which can be attributed to the further polymerization of resin with loss of water.[30] Comparing the B/P-incorporated OMCs with nonincorporated one, one can see that the three B/P-incorporated OMCs exhibited larger weight losses than the nonincorporated OMC during the second stage, which should be caused by the dehydration of boric acid or/and phosphoric acid. The

(30) Fitzer, E. *Angew. Chem., Int. Ed.* **1980**, *19*, 375.

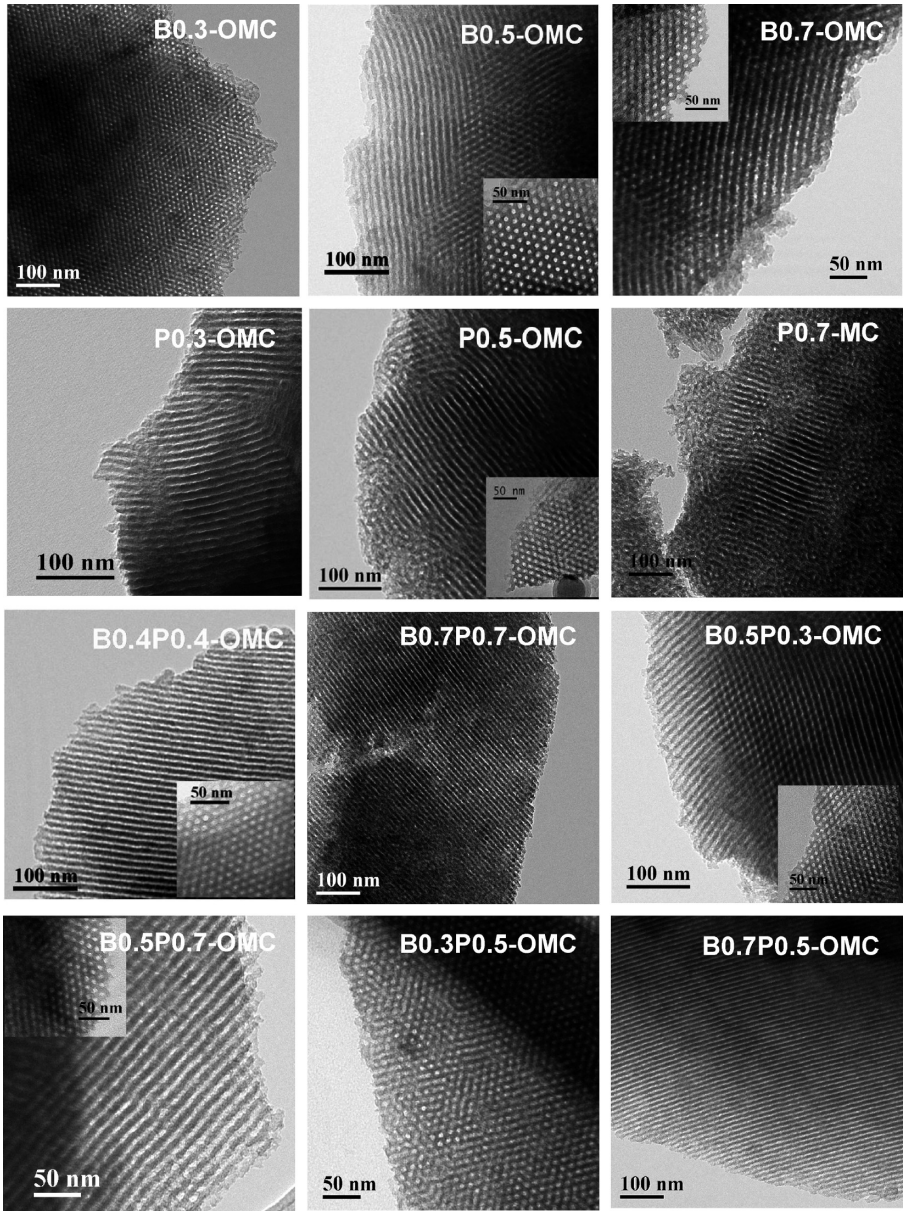

Figure 5. TEM images of B*m*-OMCs, P*n*-OMCs, and B*m*P*n*-OMCs.

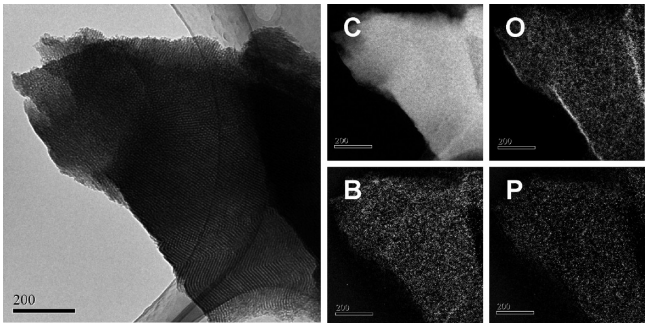

Figure 6. EELS mapping images of B, P, O, and C in the B0.5P0.5-OMC sample. The scale bars are 200 nm.

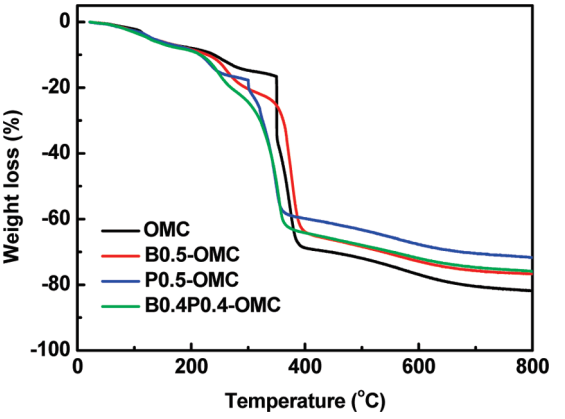

Figure 7. TG profiles of OMC, B0.5-OMC, P0.5-OMC, and B0.4P0.4-OMC in N_2 at a heating rate of 2 °C/min.

third weight loss stage was between 320 and 400 °C and was due to decomposition of surfactant F127 and the fourth stage happened between 400 and 800 °C with continuous weight losses due to pyrolysis of resin polymer into carbon. It is noted that the weight loss due to decomposition of surfactant is remarkably lower for the B/P-incorporated OMCs, suggesting that less surfactant

Table 2. Effect of Synthesis Parameters on the B Contents and Structuring Ordering of B0.5-MCs[a]

sample	temp. (°C)	F127 (g)	HCl (g)	aging time (h)	S_{BET} (m^2/g)	V_p (cm^3/g)	D_p (nm)	content of B (wt %)	ordering [b]
B-MC	Rt.	2.5	0.8	96	707	0.60	5.0	0.32	Y
B-MC-1	Rt.	2	0.6	96	688	0.59	4.8	0.30	Y
B-MC-2	Rt.	3	0.6	96	719	0.71	5.3	0.42	Y
B-MC-3	Rt.	4	0.6	96	663	0.74	6.5	0.62	N
B-MC-4	Rt.	3	0.3	96	681	0.67	5.2	0.69	N
B-MC-5	Rt.	3	1.2	96	578	0.56	4.9	0.18	Y
B-MC-6	Rt.	3	0.6	48	673	0.69	5.8	0.85	N
B-MC-7	60	3	0.6	96	664	0.63	5.2	0.35	Y

[a] The nomination of B-MC-X is used to number the samples, whereas the ordering of each sample is marked at the end of each row. [b] Y represents ordered, N represents disordered.

Table 3. Effect of Synthesis Parameters on the P Contents and Structuring Ordering of P0.5-MCs[a]

sample	temp. (°C)	F127 (g)	HCl (g)	aging time (h)	S_{BET} (m^2/g)	V_p (cm^3/g)	D_p (nm)	content of P (wt %)	ordering [b]
P-MC	Rt.	2.5	0.8	96	610	0.57	5.9	1.42	Y
P-MC-1	Rt.	2	0.6	96	651	0.58	5.5	1.21	N
P-MC-2	Rt.	3	0.6	96	684	0.67	5.8	1.51	Y
P-MC-3	Rt.	4	0.6	96	644	0.69	6.6	2.19	N
P-MC-4	Rt.	3	0.3	96	641	0.64	6.2	1.59	N
P-MC-5	Rt.	3	1.2	96	677	0.63	5.8	1.29	Y
P-MC-6	Rt.	3	0.6	48	608	0.72	7.7	1.98	N
P-MC-7	60	3	0.6	96	645	0.59	5.7	1.33	Y

[a] The nomination of P-MC-X is used to number the samples, whereas the ordering of each sample is marked at the end of each row. [b] Y represents ordered, N represents disordered.

Table 4. Effect of Synthesis Parameters on the Heteroatoms Contents and Structuring Ordering of B0.5P0.5-MCs[a]

								content (wt %)		
sample	temp. (°C)	F127 (g)	HCl (g)	aging time (h)	S_{BET} (m^2/g)	V_p (cm^3/g)	D_p (nm)	B	P	ordering [b]
BP-MC-1	Rt.	2	0.6	96	642	0.59	5.1	0.44	1.33	N
BP-MC-2	Rt.	3	0.6	96	677	0.66	4.9	0.67	2.29	Y
BP-MC-3	Rt.	4	0.6	96	525	0.59	5.4	0.59	2.04	Y
BP-MC-4	Rt.	3	0.3	96	672	0.67	5.0	0.61	1.73	Y
BP-MC-5	Rt.	3	1.2	96	623	0.57	4.8	0.48	1.61	Y
BP-MC-6	Rt.	3	0.6	48	674	0.64	4.9	0.67	2.02	Y
BP-MC-7	60	3	0.6	96	495	0.46	5.2	0.89	2.86	Y

[a] The nomination of BP-MC-X is used to number the samples, whereas the ordering of each sample is marked at the end of each row. [b] Y represents ordered, N represents disordered.

is contained in the as-synthesized heteroatom-incorporated materials. Moreover, the weight losses of the B/P-incorporated OMCs above 400 °C are also smaller than that of nonincorporated one. The less weight loss during the removal of surfactant as well as during the pyrolysis of resin contributes to the less framework shrinkage of B/P-incorporated OMCs. In addition, the decomposition of copolymer F127 seems to take place at a lower temperature for the P-containing samples, possibly because of more active oxygen being provided along with the introduction of P;[8] this was confirmed by our XPS examinations (Table 5).

Investigation of Synthesis Parameters. The above results have shown that the heteroatoms B and/or P could be incorporated into the mesoporous carbons via an aqueous phase self-assembly process. To get a comprehensive understanding of the self-assembly mechanism, we further made detailed investigations on the synthesis parameters affecting the amount of B/P incorporated into the mesoporous carbons. The effects of synthesis parameters, including reaction temperature, aging time, the amount of F127, and the amount of HCl on the contents of B and/or P in the mesoporous carbons, as well as on the ordering of mesoporous structures, have been summarized in Tables 2−4. From Tables 2 and 3, one can see that the contents of B and P in the resulting B0.5-MC and P0.5-MC materials increased with increasing amounts of F127 in the reaction mixture. On the other hand, increasing the amount of HCl led to a decrease in the contents of B and P. The aging time also had influences on the amount of B and P incorporated into the carbons. The longer the aging time, the lower the content of B or P in the carbons. However, ordered mesoporous structures could not be produced with a shorter aging time. Therefore, an aging time of 96 h was employed in our typical syntheses. Finally, the effect of reaction temperature was investigated. It was found that increasing the reaction temperature from RT to 60 °C brought about a decrease in the content of B or P in the resulting carbons.

In the case of B, P-coincorporation, the effects of the above parameters are slightly different from the case of solo-incorporation. As shown in Table 4, when the reaction temperature was raised from RT to 60 °C, more amounts of B and P were incorporated into the carbon material. Moreover, both F127 and HCl had an optimum amount at which the highest contents of B and P were obtained.

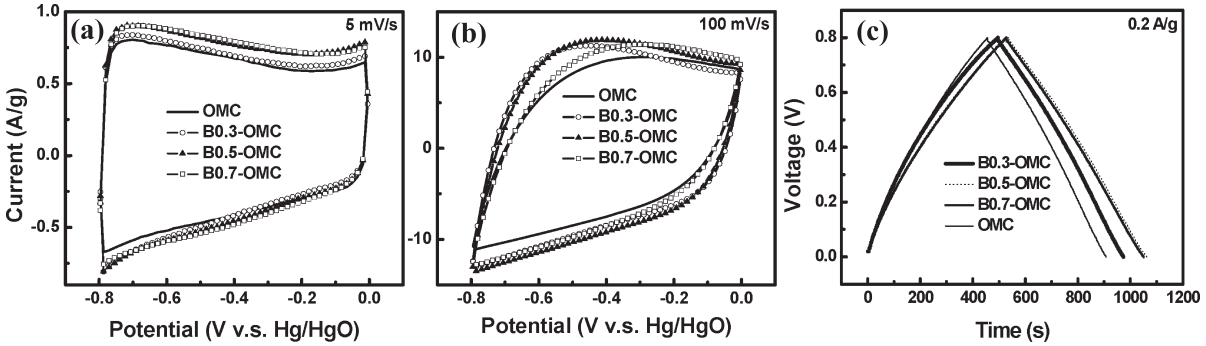

Figure 8. CV curves measured at (a) 5 and (b) 100 mV/s and (c) GC profiles at current density of 0.2 A/g of B*m*-OMCs.

Scheme 1. Proposed Mechanism for Multicomponent Self-Assembly of Resorcinol, Formaldehyde, F127, and B or/and P Precursors

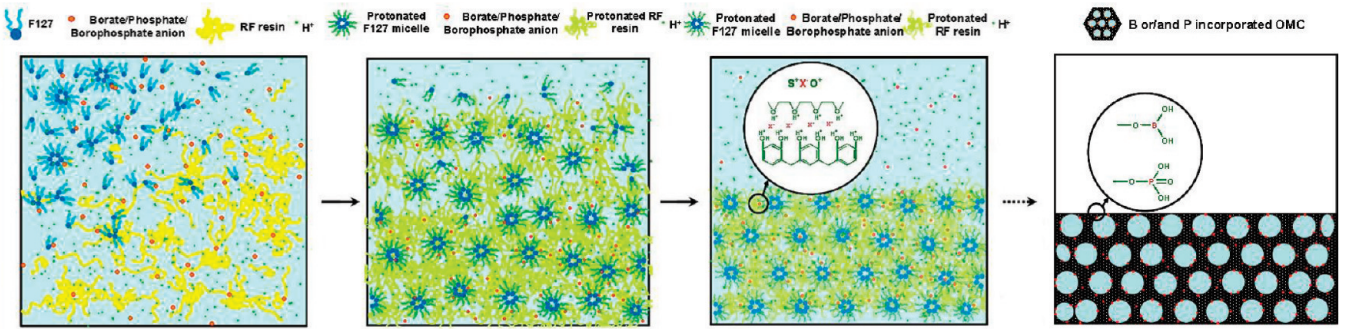

Because acidic conditions may favor the protonation of phenols, cross-linked phenols, and the EO blocks of F127, Wang et al. proposed that the self-assembly process of resorcinol-formaldehyde and block copolymers under strongly acidic conditions was probably driven by Coulombic interactions via the $I^+X^-S^+$ mechanism.[18] According to this mechanism, when solo-element B or P is introduced into the resorcinol-formaldehyde mixture, the borate or phosphate anions will coassemble with the protonated phenolic polymer and F127, as illustrated in scheme 1. In this case, more amount of F127 will incorporate more amount of borate or phosphate anions, while more HCl (the Cl^- anions) will compete with borate or phosphate anions and lead to decreased amount of B or P incorporated. Clearly, this mechanism is in good agreement with our experimental results. In the case of cointroduction of both B and P, borophosphate anions like $[B_xP_yO_z]^{n-}$ may be formed and assembled with phenolic polymer and F127. It was reported that borophosphate anions could be formed even at RT and atmospheric pressure.[31] Moreover, our wide-angle XRD examinations also showed the formation of BPO_4 upon calcining the B, P-containing polymer at 350 °C. Because of the interaction between B and P species, the amounts of B and P incorporated into the carbon materials were markedly enhanced in comparison with the case of solo-element incorporation. The experimental fact that a higher reaction temperature (e.g., 60 °C) favored more amounts of B and P incorporated into the materials also suggests that the formation rate of borophosphate anions is accelerated with increasing temperature.

(31) Ge, M. H.; Liu, W.; Li, M. R.; Yang, X. X.; Chen, H. H.; Zhao, J. T. *Chin. J. Inorg. Chem.* **2005**, *21*, 826.

Electrochemical Properties. The above heteroatom-incorporated OMCs synthesized under typical conditions (the samples in Table 1) were subsequently evaluated as the electrodes of supercapacitors. Figures 8−10 show the cyclic voltammetry (CV) curves of the B*m*-OMCs, P*n*-OMCs, and B*m*P*n*-OMCs at scan rates of 5 and 100 mV/s in 6 M KOH electrolyte, as well as the galvanostatic charge−discharge (GC) profiles at a current density of 0.2 A/g. At a low scan rate of 5 mV/s, both the heteroatom-incorporated OMCs and the nonincorporated OMC present well-symmetric and rectangular CV curves, indicating ideal electric double-layer capacitor (EDLC) performances. However, at a high scan rate of 100 mV/s, more critical for evaluating the capacitor performance, the CV curves of both the OMC and P*n*-OMCs are no longer rectangular. In contrast, the rectangular and symmetric characteristics can still be preserved in B*m*-OMCs and B*m*P*n*-OMCs. This result suggests that the capacitor performance of the OMC at high-rate discharge or recharge can be substantially improved by incorporation of B. To further demonstrate this point, CV tests at different scan rates were conducted on different heteroatom-incorporated OMCs. In Figure 11, the calculated capacitance retention ratios of OMC, B0.5-OMC, P0.5-OMC, and B0.4P0.4-OMC as a function of the potential scan rate are illustrated. As a reference, the retention performance of the commercial active carbon (Norit) is also shown in Figure 11. When the scan rate was increased from 2 to 100 mV/s, the capacitance retention of Norit carbon was only 49%, which is significantly lower than the OMC and heteroatom-incorporated OMCs. More intriguing, the capacitance retentions of B0.5-OMC and B0.4P0.4-OMC were 68 and 73%, respectively, which are increased by more than 20% over that of the Norit carbon. Obviously, the incorporation

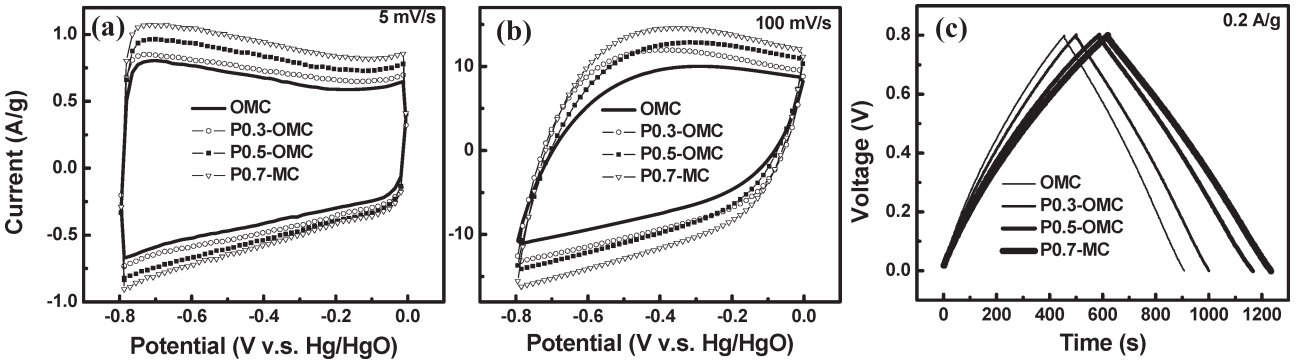

Figure 9. CV curves measured at (a) 5 and (b) 100 mV/s and (c) GC profiles at current density of 0.2 A/g of P*n*-OMCs.

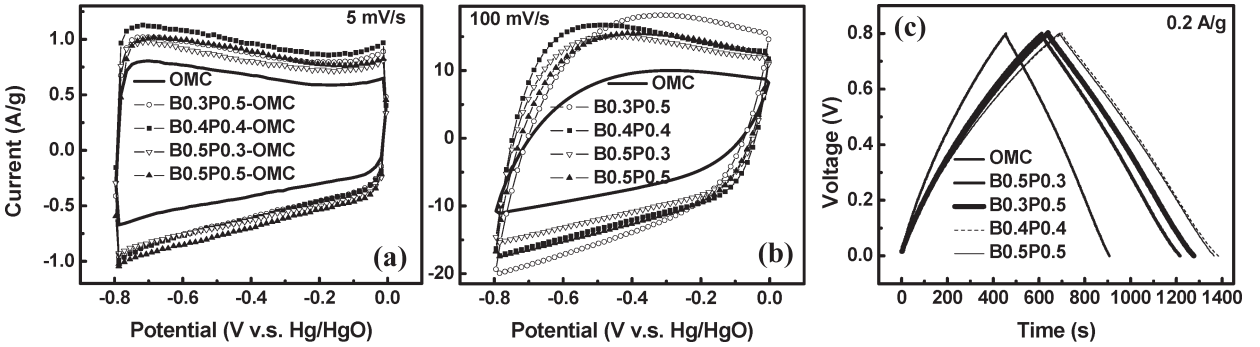

Figure 10. CV curves measured at (a) 5 and (b) 100 mV/s and (c) GC profiles at current density of 0.2 A/g of B*m*P*n*-OMCs.

of B into the framework of OMC remarkably improved the capacitance performance of electrodes at high scan rates, and this is very important for the applications where high-rate discharge−recharge is required. In addition, incorporation of P or B also results in the enhancement of specific capacitance of OMC. As shown in Figures 8−10, the forward and reverse current densities of the heteroatom-incorporated OMCs increase with the amount of B and/or P. To demonstrate this point clearly, we calculated the specific capacitance per single electrode according to GC test at a current of 0.2 A/g, and the results are summarized in Table 1. It can be seen that the blank OMC has a comparable specific capacitance to the Norit carbon. However, upon incorporation of B or P, the specific capacitances of the solo-incorporated materials are increased. It was found that the incorporation of B results in only a slight increase in the specific capacitance. On the other hand, incorporation of P led to a large increase in specific capacitance, from 0.16 F/m^2 (OMC) to 0.28 F/m^2 (P0.7-MC). However, because of the decrease in specific surface areas accompanied with the incorporation of P, the specific capacitance per gram of carbon was not the highest for the P0.7-MC. For a series of B*m*P*n*-OMCs, the specific capacitances varied from 0.22 to 0.28 F/m^2 depending on the actual contents of B and P. For example, at a fixed m value ($m = 0.5$), the specific capacitances changed from 0.22 to 0.28 F/m^2 when the n value changed from 0.3 to 0.7. On the other hand, keeping n at a constant value ($n = 0.5$), the specific capacitance remained almost unchanged (0.25 F/m^2) with increasing m value. It seems that there is not a consistent trend between the specific capacitance and the actual contents of B and P for the B*m*P*n*-OMCs. Actually, we found that the B0.4P0.4-OMC,

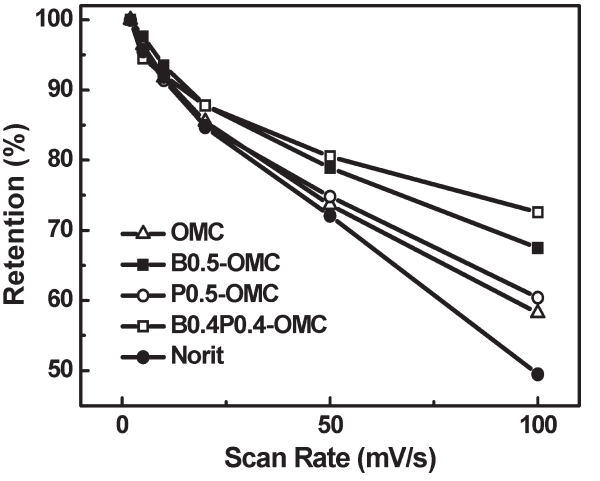

Figure 11. Capacitance retention ratio as a function of the potential scan rates of OMC, B0.5-OMC, P0.5-OMC, and B0.4P0.4-OMC.

which balanced the heteroatoms concentrations and the surface area, exhibited the best capacitance performance in terms of specific capacitance per gram of carbon (172 F/g) and the capacitance retention at a high scan rate (approximately 1.60 and 1.94 times that of OMC at a scan rate of 2 and 100 mV/s, respectively).

Correlation between the Electrochemical Property and the Surface Functionalities. To reveal the reason for the superior double layer capacitance of the heteroatom-incorporated OMCs to the nonincorporated one, we select B0.5-OMC, P0.5-OMC, and B0.4P0.4-OMC as the representatives of these heteroatom-incorporated samples to conduct XPS and thus probe the chemical state of

Table 5. XPS Results of OMC and Heteroatom-Incorporated OMCs

	binding energy (eV)				elemental content (wt %)			
sample	P_{2P}	B_{1S}	O_{1S} (=O)	O_{1S} (−O−)	B	P	O	intensity ratio I(−O−)/I(=O)[a]
OMC			532.2	533.6			8.48	0.71
B0.5-OMC		192.2	531.9	533.2	0.44		10.27	2.47
P0.5-OMC	132.9		531.0	532.7		1.49	12.90	0.80
B0.4P0.4-OMC	132.8	192.0	531.5	532.9	0.69	2.23	10.89	2.51

[a] Calculated as the ratio of the fitted area of −O− peak to the fitted area of =O peak.

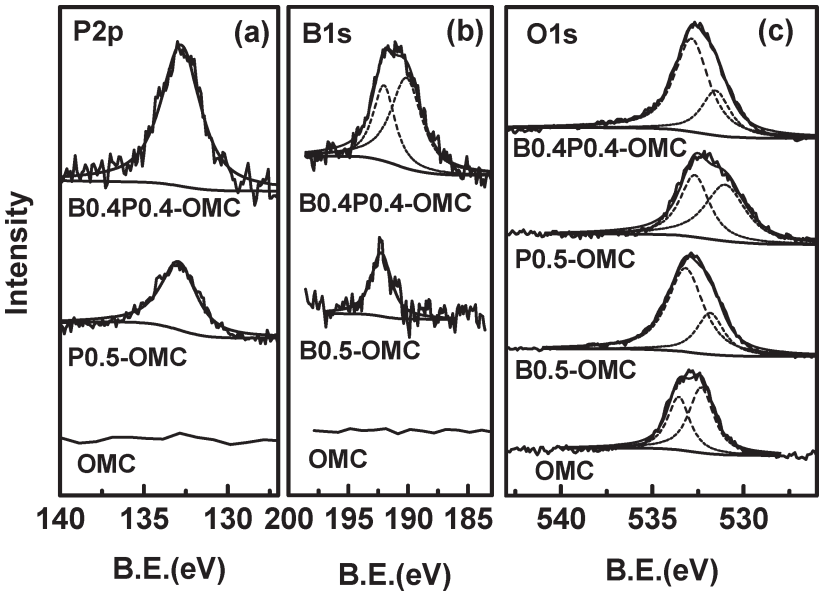

Figure 12. XPS spectra of (a) P_{2p}, (b) B_{1s}, (c) O_{1s} for OMC, B0.5-OMC, P0.5-OMC, and B0.4P0.4-OMC. It is noted that the B1s peak of B0.4P0.4-OMC is overlapped with P2s.[36]

heteroatoms in the carbon framework. As shown in Table 5, the surface compositions of the doped heteroatoms detected by XPS are slightly higher than those determined by ICP, suggesting that some surface enrichment of B and P occurred. Furthermore, from the XPS spectra (Figure 12), one can clearly see that the binding energy of B_{1s}, either in the B0.5-OMC or in the B0.4P0.4-OMC, centered at 192.0−192.2 eV, which can be attributed to B−O−C or B−O−P.[19,32] Similarly, the P_{2P} has a binding energy of 132.8−132.9 eV, which can be assigned to P−O−C or P−O−B in both P-containing OMC samples.[32,33] Along with the incorporation of heteroatoms into the carbon framework, the surface oxygen content has an apparent increase, as shown in Table 5. Compared with OMC, a clear shift to lower binding energy and a broaden tendency are observed in the O_{1s} spectra of the heteroatom-incorporated OMCs, particularly for the P-OMCs (Figure 11). To identify different oxygen species, we deconvoluted the O_{1s} spectra into two peaks attributable to bridge-bonded oxygen (−O−, 533.6−532.7 eV) and double-bonded oxygen (=O, 532.2−531.0 eV),[34] respectively. Moreover, the relative intensity of the two oxygen species (I(−O−)/I(=O)) increases significantly with the incorporation of heteroatom B. In combination with the electrochemical properties, we can assume that increasing single-bonded oxygen groups on the carbon surface, for example, via incorporating B, benefits for the capacitance retention at a high scan rate, although the reason is not clear yet.

Very recently, Kwon et al. investigated the capacitance enhancement mechanisms caused by N- or B-doping,[35] and they concluded that the pseudocapacitance through faradic charge transfer is the main reason for the enhancement of capacitance by doping of N and B. In our case, the incorporation of P or/and B into the carbon framework not only produced the heteroatom functional groups on the carbon surface, but also yielded additional surface oxygen groups. These functional groups are believed to conduct complex faradic reactions with a wide range of beginning potentials and thus enhance the pseudocapacitance, although no any sharp peak was observed in the CV curves of the doped OMCs. On the other hand, accompanied with the introduction of B or/and P, the pore structure of OMC is also affected, as indicated by the changes of specific surface areas and average pore sizes. Recently, it was reported that the

(32) Raskar, D.; Rinke, M. T.; Eckert, H. *J. Phys. Chem. C* **2008**, *112*, 12530.
(33) Puziy, A. M.; Poddubnaya, O. I.; Socha, R. P.; Gurgul, J.; Wisniewski, M. *Carbon* **2008**, *46*, 2113.
(34) Wang, Y. Q.; Zhang, F. Q.; Sherwood, P. M. A. *Chem. Mater.* **2001**, *13*, 832.
(35) Kwon, T.; Nishihara, H.; Itoi, H.; Yang, Q. H.; Kyotani, T. *Langmuir* **2009**, *25*, 11961.
(36) Wagner, C. D.; Riggs, W. M.; Davis, L. E.; Moulder, J. F.; Muilenberg, G. E., *Handbook of X-ray Photoelectron Spectroscopy*; Perkin-Elmer Corporation: New York, 1979.

desolvation of electrolyte ions in subnanometer pores led to higher capacitance.[2,37] To determine whether the micropores in heteroatom-incorporated OMCs contribute to the enhanced capacitance, we measured the micropore size distributions of the materials. The results showed that the micropore sizes of these samples were all centered at 0.6 nm regardless of the heteroatom concentration. This value is much smaller than the optimum pore size (0.7−0.8 nm) of carbon-based electrodes for EDLC capacitance. Therefore, the contribution of micropores of the heteroatom-incorporated OMCs is not considered here. However, the surface areas and the mesopores are indeed changed with the incorporation of heteroatoms, which can bring about the changes in the capacitance performance of the carbon materials. Through simultaneous incorporation of B and P into the carbon framework, the functional groups including boron, phosphorus, and oxygen on the carbon surface are increased and meanwhile the large specific surface area of the OMC is maintained, as a result, the specific capacitance and the capacitance retention at a high potential scan rate are greatly enhanced.

(37) Largeot, C.; Portet, C.; Chmiola, J.; Taberna, P. L.; Gogotsi, Y.; Simon, P. *J. Am. Chem. Soc.* **2008**, *130*, 2730.

Conclusions

In conclusion, we have developed a facile one-pot method to incorporate heteroatoms into carbon framework while maintaining the well-ordered mesoporous structure. The resulting heteroatom-incorporated OMCs (B-incorporated, P-incorporated, and B, P-coincorporated OMCs) exhibited superior electrochemical performances to the nonincorporated counterpart when they were used as electrodes of supercapacitors. In particular, the B, P-coincorporated OMCs showed promising capacitance performance at a high scan rate. This method can be further extended to synthesis of other heteroatom-incorporated OMCs, and future work should be focused on increasing the concentration of heteroatoms as well as enlarging the surface areas of OMCs.

Acknowledgment. We gratefully acknowledge the financial support of the National Basic Research Program of China (2009CB226102).

Supporting Information Available: Micropore size distribution (PDF). This material is available free of charge via the Internet at http://pubs.acs.org/.